

This document is confidential and is proprietary to the American Chemical Society and its authors. Do not copy or disclose without written permission. If you have received this item in error, notify the sender and delete all copies.

Harnessing Atomic Layer Deposition and Diffusion to Spatially Localize Rare-Earth Ion Emitters

Journal:	<i>The Journal of Physical Chemistry</i>
Manuscript ID	jp-2020-04019x
Manuscript Type:	Article
Date Submitted by the Author:	05-May-2020
Complete List of Authors:	Ferrier, Alban; PSL, IRCP Harada, Nao; Institut de Recherche de Chimie Paris Scarafagio, Marion; Institut de Recherche de Chimie Paris Briand, Emrick; CNRS (UMR 7588), Universités Pierre et Marie Curie et Denis Diderot, Institut des Nanosciences de Paris Ganem, jean-jacques ; Institut des NanoSciences de Paris Vickridge, Ian; Institut des NanoSciences de Paris Seyeux, Antoine ; Institut de Recherche de Chimie Paris Marcus, Philippe; Institut de Recherche de Chimie Paris Serrano, Diana; Institut de Recherche de Chimie Paris Goldner, Philippe; Institut de Recherche de Chimie Paris Tallaire, Alexandre; Institut de Recherche de Chimie Paris

SCHOLARONE™
Manuscripts

Harnessing atomic layer deposition and diffusion to spatially localize rare-earth ion emitters.

Alban Ferrier^{1,2}, Nao Harada¹, Marion Scarafagio¹, Emrick Briand⁶, Jean Jacques Ganem³, Ian Vickridge³, Antoine Seyeux¹, Philippe Marcus¹, Diana Serrano¹, Philippe Goldner¹ and Alexandre Tallaire¹*

¹ Institut de Recherche de Chimie Paris (IRCP), Université PSL, Chimie ParisTech, CNRS, 75005 Paris, France

² Sorbonne Université, Faculté des Sciences et Ingénierie, UFR 933, 75005 Paris, France

³ Sorbonne Universités, Institut des NanoSciences de Paris, INSP, 75005 Paris, France

KEYWORDS : spatial localization of emitters, atomic layer deposition (ALD), Europium diffusion, hole burning spectroscopy, quantum technologies, rutherford backscattering spectroscopy (RBS), time of flight secondary ion mass spectrometry (TOF SIMS).

*corresponding author: alban.ferrier@chimieparistech.psl.eu

1
2
3 ABSTRACT: Control of rare-earth ions doping profiles is a key challenge for several photonics
4
5
6 applications and for quantum technologies that require spatially localized emitters. Atomic Layer
7
8
9 Deposition (ALD) is a conformal method that can provide in-depth nanometer-scale positioning
10
11
12 accuracy on a large scale. However, post thermal annealing is usually needed to achieve high
13
14
15 crystalline quality, which induces unwanted dopant diffusion and partial loss of their localization.
16
17
18 In this work, we study europium ion diffusion in an ALD-grown $\text{Eu}_2\text{O}_3/\text{Y}_2\text{O}_3/\text{Si}$ stack using
19
20
21 Rutherford Backscattering Spectroscopy (RBS) and Time of Flight Secondary Ion Mass
22
23
24 Spectrometry (TOF SIMS). We then extend this approach to investigate diffusion from an Eu_2O_3
25
26
27 ALD film into a single crystalline substrate of Y_2SiO_5 (YSO), a technologically relevant material
28
29
30 system for quantum applications. We determine Eu^{3+} diffusion coefficients in both cases and show
31
32
33 that in the polycrystalline Y_2O_3 ALD sub-micron film, diffusion starts at 950 °C whereas in single
34
35
36 crystal YSO it becomes significant, only above 1200 °C. Finally, spectral hole burning of such in-
37
38
39 diffused emitters revealed homogeneous lines as narrow as 2 MHz. This study indicates that an
40
41
42 appropriate annealing of ALD-grown rare-earth oxide films can be harnessed to create localized
43
44
45 dopants that preserve their outstanding optical properties, a pre-requisite for their integration into
46
47
48 photonic and quantum devices.
49
50
51
52
53
54
55
56
57
58
59
60

1. Introduction

Lanthanide-doped oxide crystalline hosts are well known luminescent platforms for photonic applications. Indeed their unique optical properties have advanced a broad range of applications including lighting, sensors, bio-imaging or more recently Quantum Technologies (QT).¹ The development of rare-earth (RE) doped films presents several benefits as compared to bulk single crystals. For example, the use of waveguides or multilayer architectures can increase the light-matter interaction and thus device operation and sensitivity. In addition, the spatial localization of RE ions close to the surface is highly desirable for exploiting their coherent properties within a quantum device, in particular for improved coupling to a cavity or to an hybrid structure.^{2,3,4,5} For example in several quantum sensing schemes, the sensitivity scales as the square root of the number of interacting emitters while coupling to the external field to be sensed can be maximized by placing the emitters close to the surface (10s of nanometer).⁶ High emitter concentration close to the surface is required, whereas emitters inside the bulk will decrease the sensitivity since they are not affected by the surface perturbations. This near-surface doping is not accessible with classical bulk crystal growth where the dopant is inserted in the melt and is distributed according to the segregation law. Finally, lanthanide dopant concentration profiles along the film might also be of interest for optimized up-conversion or lighting.⁷

1
2
3
4 Currently, the most common technique for ion localization is ion implantation. Indeed, ion
5
6
7 implantation is a powerful approach to precisely localize atoms within a crystalline matrix at
8
9
10 controlled depths.⁸ However, implantation induces damage and defects especially when heavy
11
12
13 atoms (like lanthanides) are considered.⁹ These defects contribute to increase the spectral
14
15
16 broadening of the emitters and reduces the overall performance (e.g. larger homogeneous and
17
18
19 inhomogeneous linewidth, lower quantum efficiency).^{10,11} Furthermore the implantation yield is
20
21
22 typically less than 50 %, indicating that at least half of the implanted ions do not emit photons.
23
24
25
26 This low yield can be very detrimental for QT since decoherence rates are in general related to
27
28
29 the coupling with other spins of the matrix (e.g. in particular other implanted yet inactive ions). For
30
31
32 instance, to our knowledge, no Spectral Hole Burning (SHB) has been demonstrated on
33
34
35 lanthanide-implanted single crystals. However, SHB is a key requirement in QT for the quantum
36
37
38 states initialization by allowing spectral tailoring of the inhomogeneous absorption profile by
39
40
41 efficient population transfer between ground-state hyperfine levels using optical pumping.¹
42
43
44
45 Therefore, other strategies that preserve ion properties while allowing high localization efficiency
46
47
48 are desirable.
49

50
51
52 Atomic Layer Deposition (ALD) is highly suited for precisely controlling the composition and
53
54
55 nanoscale in-depth positioning of dopants in a thin film. Indeed, the sequential injection of
56
57
58
59
60

1
2
3 precursors enables a slow layer-by-layer growth mode with a high flexibility. It offers large wafer-
4
5
6 scale process-ability as well as deposition on complex nanostructures. The use of appropriate
7
8
9 ligands with large steric hindrance can increase the distance between RE ions in the lateral
10
11
12 direction thus improving in-plane positioning as well.^{7,12,13} Recently, we demonstrated for ALD-
13
14
15 grown Eu³⁺-doped Y₂O₃ thin films using Y(tmhd)₃ and ozone as precursors that a high deposition
16
17
18 temperature (350 °C) and post treatment annealing above 900°C are key parameters for
19
20
21 optimizing the luminescent properties.¹⁴ In fact, by improving the crystalline environment of the
22
23
24 ions, inhomogeneous lines of 200 GHz were obtained for the ⁷F₀ → ⁵D₀ transition of Eu³⁺ even for
25
26
27 nanoscale films (thickness < 100 nm) which is a promising first step towards their integration in
28
29
30 QTs. One obvious drawback of this approach is related to the fact that at such a high annealing
31
32
33 temperature, RE dopants are mobile and can interact at the interface with silicon. Too high
34
35
36 annealing temperature induces a modification of the spatial distribution of RE ions, as well as
37
38
39 formation of a silicate phase at the interface.¹⁴ These are detrimental to the precise positioning of
40
41
42 emitters as well as the control of their environment. Phase mixing indeed affects the frequency
43
44
45 range of ions' emission, leads to strong inhomogeneous broadening and increases the dephasing
46
47
48 processes rate by disorder mode.^{15,16}
49
50
51
52
53
54
55
56
57
58
59
60

1
2
3 Diffusion of lanthanide ions in single crystals or ceramics like Al_2O_3 , $\text{Y}_3\text{Al}_5\text{O}_{12}$ or YVO_4 has been
4
5
6 reported for a large range of applications including mineralogy, waveguide fabrication or ceramic
7
8
9 sintering.^{17,18,19,20,21} For photonics, thermal diffusion of transition metals has been extensively
10
11
12 studied to form low-cost waveguides in LiNbO_3 .²² In that case, the transition metal ion acts as a
13
14
15 local refractive index modifier leading to passive waveguides. Further works have demonstrated
16
17
18 that thermal diffusion is also a useful approach for RE doping in oxide single crystals for laser
19
20
21 applications.¹¹ However, only scarce data exists on diffusion in nanometer-scale films obtained
22
23
24 by ALD or more generally about ions' redistribution during thermal annealing.²³ Annealing
25
26
27 temperature and duration need to be carefully optimized in order to preserve dopant localization
28
29
30 or to harness their diffusion, as well as to avoid unwanted phases formation.
31
32
33

34
35
36 In this study, we focus on the diffusion of Eu^{3+} cations during thermal annealing using Rutherford
37
38
39 Backscattering Spectroscopy (RBS) and Time of Flight Secondary Ion Mass Spectrometry (TOF
40
41
42 SIMS). We first study Eu^{3+} diffusion in an ALD-grown $\text{Eu}_2\text{O}_3/\text{Y}_2\text{O}_3/\text{Si}$ (100) stack in the 600-
43
44
45 1000 °C range (Fig. 1a) from which we determine the diffusion coefficient as well as investigate
46
47
48 the reactivity at the interface. This multilayer presents the advantage of being directly grown by
49
50
51 ALD on a standard low cost and large area Si wafer but possesses limited crystallinity. We then
52
53
54 extend this study to Eu^{3+} diffusion from an ALD-grown Eu_2O_3 layer above a bulk Y_2SiO_5 (YSO)
55
56
57
58
59
60

single crystalline substrate grown by crystal pulling (Fig. 1b) which is the most common host crystal used for RE based QTs.¹ In this latter case, we demonstrate that diffusion at higher temperatures (1000-1500 °C) can be explored as an alternative to ion implantation in order to create localized RE ions close to the YSO surface, within the first 200 nm. We observe SHB from such in-diffused ions and measure a promising hole linewidth of 4 MHz. This indicates that this strategy is suitable to engineer materials that could provide a suitable platform for QTs.

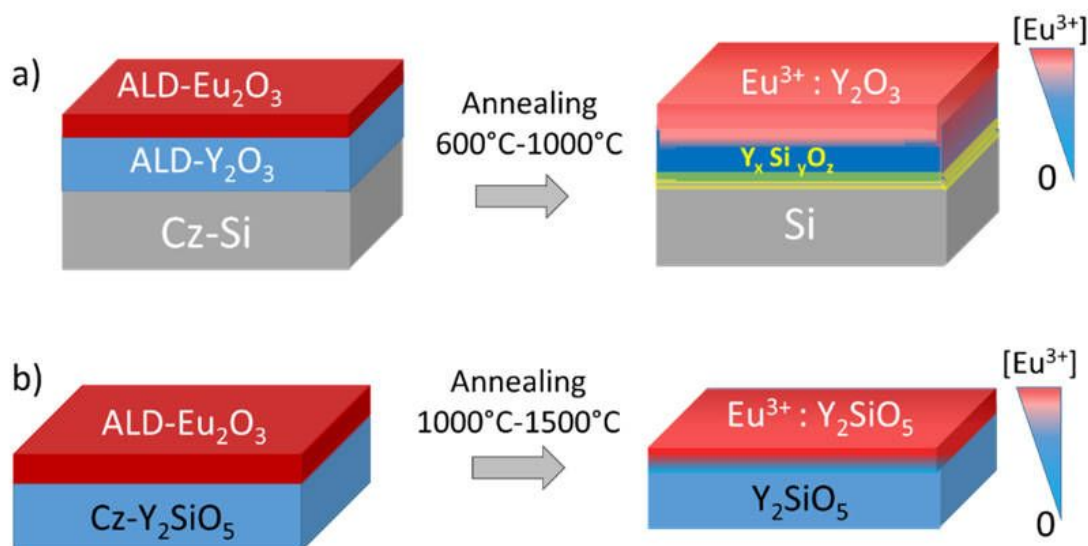


Figure 1: Schematic representation of the two sets of samples investigated. a) Diffusion of Eu^{3+} from a Eu_2O_3 layer (typically 15 to 20 nm thick) on Y_2O_3 (120 nm thick). The two layers were deposited by ALD on silicon (100). b) Diffusion of Eu^{3+} from a Eu_2O_3 layer (20 nm thick) deposited

1
2
3 on a thick *b*-oriented single crystalline YSO substrate (010) grown by a crystal pulling technique
4
5
6 and optically polished.
7
8
9

10 2. Experimental section

11
12
13
14
15 Eu₂O₃ and Y₂O₃ film depositions were carried out by ALD with a *Picosun Sunale R200* using
16
17
18 conventional β-diketonate precursors: Eu(tmhd)₃ and Y(tmhd)₃ (99.9 % purity from *Strem*
19
20
21 *Chemicals*). The precursors were held at 160°C and delivered using 300 sccm N₂ as a carrier
22
23
24 gas. Ozone (O₃) was used as a strong oxidizing agent. The precursors were flown sequentially
25
26
27
28 with 3s injection time into the thermalized deposition chamber at 350 °C. The number of cycles
29
30
31 was adjusted in order to obtain the desired thickness. More details about the impact of the different
32
33
34 deposition parameters and their optimization are discussed in Scarafagio et al.¹⁴ For the
35
36
37 Eu₂O₃/Y₂O₃/Si stack, a first 120 nm-thick Y₂O₃ layer was grown on a Si (100) wafer covered by a
38
39
40 native oxide (SiO₂). It was annealed for 2 h at 900 °C in air before a 15 nm thick Eu₂O₃ layer was
41
42
43
44 grown (see Fig. 1a). In this second deposition, a slight thickness variation of the Eu₂O₃ layer is
45
46
47
48 observed from sample to sample. This thickness variation is possibly due to slightly varying
49
50
51 growth conditions and positioning inside the reactor chamber but it does not notably change the
52
53
54 diffusion profile.
55
56
57
58
59
60

1
2
3 For the $\text{Eu}_2\text{O}_3/\text{Y}_2\text{SiO}_5$ stack, a 20 nm-thick layer was directly deposited by ALD on a specially
4
5
6 prepared single crystalline substrate (see Fig. 1b). YSO was grown by Czochralski method (Cz)
7
8
9 along the b direction following the procedure described by Ferrier et al.²⁴ After crystal orientation
10
11
12 by the Laue method, it was cut and optically polished perpendicularly to the b direction.
13
14
15

16
17 Film thickness was estimated by white light interferometry in the range 250-1000 nm with an
18
19
20 *Ocean Optics NanoCalc* and an *ISE Woollam* spectroscopic ellipsometer system. Eu_2O_3 and Y_2O_3
21
22
23 optical constants have been fitted using a Cauchy model. Thermal annealing was performed in
24
25
26 air in the range 600-1500 °C for 2 h in order to activate europium diffusion from the top layer into
27
28
29 the layer beneath.
30
31
32

33
34 RBS and TOF-SIMS bring complementary information and are both explored here to assess Eu^{3+}
35
36
37 diffusion mechanisms. Indeed, RBS is non-destructive and provides quantitative atomic
38
39
40 composition with a 10 nm in-depth resolution whereas TOF SIMS is used to determine with high
41
42
43 accuracy (less than 1 nm) the depth profiling of different elements.
44
45
46

47
48 Ion beam analyses were carried out using the Van de Graaf accelerator of the SAFIR Platform of
49
50
51 Sorbonne Université. RBS was performed with 1800 keV $^4\text{He}^+$ beam in a non-channeling
52
53
54 geometry. In RBS, the energy of the backscattered ions depends on both the element with which
55
56
57
58
59
60

1
2
3 the ion experienced an elastic collision as well as its depth positioning within the target material.
4
5

6 In addition, the area of the peak related to an element is proportional to the atomic density of this
7
8
9
10 element in the material. To determine the concentration profile, a simulation was carried out using
11
12
13 the SIMNRA software.²⁵ First, the experimental parameters (ion energy, geometry of the
14
15
16 experiments and channel to energy conversion) are introduced in the model and carefully checked
17
18
19 using a reference target (in our case Bi ions implanted in silicon). Then the substrate is modelled
20
21
22 as a N sublayers of adjusted composition in order to obtain the best fit of the experimental RBS
23
24
25 spectrum. In the case of uniform distribution, only one sublayer is used whereas a non-uniform
26
27
28 distribution of elements is refined with N sublayers with gradual variation of the composition. The
29
30
31 thicknesses of each sublayers are determined afterwards using the following formula:
32
33

$$d = \frac{MA}{\rho N_A} \quad (\text{eq. 1})$$

34
35
36
37
38
39
40 Where d is the thickness of the sublayer, A is the areal density, M the molecular mass calculated
41
42
43 with the determined composition ($Y_xEu_yO_z$), N_A the Avogadro constant and ρ the density. The
44
45
46 density of Eu^{3+} doped Y_2O_3 has been estimated by linear interpolation from the two values of the
47
48
49 pure compounds (5.3 g cm^{-3} and 7.02 g cm^{-3} for Y_2O_3 and Eu_2O_3 respectively). Furthermore, as
50
51
52 we used a silicon substrate, the precise determination of elements lighter than silicon by RBS is
53
54
55

1
2
3 more complicated. That's why for $\text{Eu}_2\text{O}_3/\text{Y}_2\text{O}_3/\text{Si}$, the oxygen areal densities were also determined
4
5
6 by nuclear reaction analysis (NRA) using the $^{16}\text{O}(\text{d},\text{p})^{12}\text{C}$ reaction induced by a deuteron beam of
7
8
9
10 850 keV and a detection angle of 150° . Indeed, this nuclear reaction is specific to oxygen allowing
11
12
13 quantification by a simple integration of the proton peaks on the NRA spectrum (see Figure S1).
14
15
16 Then, comparison of those integrated values with two standards of Ta_2O_5 allowed precise
17
18
19 determination of the oxygen composition of the thin film. Good agreement was obtained between
20
21
22 the O content extracted from RBS and NRA studies with typical variation of about 2 %.
23
24
25

26
27 The in-depth concentration profiles were also studied using the dual-beam TOF-SIMS V
28
29 spectrometer (*ION-TOF GmbH, Muenster, Germany*) of the Physical Chemistry of Surfaces
30
31
32 Group at IRCP Chimie Paristech. Indeed, we measured the concentration depth profile of the
33
34
35 yttrium and erbium ions at a sufficiently low primary ion dose density to keep static conditions.
36
37
38 Charge compensation was performed by using an electron flood gun. The spectrometer was
39
40
41 operated at a pressure of 10^{-9} mbar. A pulsed 25 kV Bi^+ primary ion beam delivering 1 pA over a
42
43
44
45
46 $100 \times 100 \mu\text{m}^2$ area is used to extract the chemical species from the surface. The masses of the
47
48
49 removed chemical species are determined by time-of-flight mass spectroscopy. The sputtering of
50
51
52 the surface was done using a 2 keV Cs^+ sputter gun giving a 100 nA target current over a
53
54
55
56 $300 \times 300 \mu\text{m}^2$ area. The interlacing between Bi^+ and Cs^+ guns allows to record TOF-SIMS depth
57
58
59
60

1
2
3 profiles. Analysis was centered inside the sputtered crater to avoid edge effects. Data acquisition
4
5
6 and post-processing were carried out using *Surface Lab 6.7* software. The sputter profiles were
7
8
9 converted into depth by measuring the crater's depth with a surface profiler (*Dektak 150, Veeco*),
10
11
12 assuming a constant sputtering rate. The main uncertainty of this data results from the limited
13
14
15 accuracy of the depth scaling. TOF-SIMS is destructive but is well adapted to determine dopant
16
17
18 concentration profiles being done with accuracy better than 1 nm. TOF-SIMS requires precisely
19
20
21 calibrated standards and is function of the analyzed matrix for quantitative assessment since the
22
23
24 ionization yield of each element is generally different. Eu and Y contributions were assessed by
25
26
27 following EuO_2^- and YO^- sputtered ions signals. Contribution from other elements (SiO^- , C and Si)
28
29
30 were also analyzed but will not be discussed in detail in this paper. In particular, the precise
31
32
33 determination of the top layer's thickness was difficult due to the roughness induced by the
34
35
36 annealing post treatment.
37
38
39

40
41
42 Finally, SHB experiments were performed with a home-made low temperature microscope using
43
44
45 a high numerical aperture lens on a nano-positionner (See Supporting information for more details
46
47
48 and Figure S5). Briefly, samples were introduced into a He bath cryostat (*Janis SVT-200*). The
49
50
51 temperature was monitored directly on the sample-holder by a Si diode (*Lakeshore DT-670*). A
52
53
54 continuous wave (CW) dye laser (*Sirah Matisse DS*) with 300 kHz linewidth provided the optical
55
56
57
58
59
60

1
2
3 excitation around 580 nm. Pulsed sequences required for SHB measurements were created by
4
5
6 modulating the CW laser with one acousto-optic modulator driven by an arbitrary waveform
7
8
9 generator (*Agilent N8242A*). The red luminescence was filtered using band-pass and interferential
10
11
12 filters and sent to a high sensitivity photomultiplier (*PMT R10699 Thorlabs*).
13
14
15

16 17 **3. Results and discussion**

18 19 20 21 **3.1. Eu^{3+} diffusion in an ALD-grown $\text{Eu}_2\text{O}_3/\text{Y}_2\text{O}_3/\text{Si}$ (100) stack**

22
23
24
25 We first focus on reactions occurring at the substrate/layer interface of the ALD-grown
26
27
28 polycrystalline $\text{Eu}_2\text{O}_3/\text{Y}_2\text{O}_3/\text{Si}$ (100) stack during thermal annealing. Typical RBS spectra for 2
29
30
31 different annealing temperatures are presented in Fig. 2. The contribution from silicon, oxygen,
32
33
34 yttrium and europium are clearly visible. No additional elements appear on the RBS spectrum
35
36
37 indicating no obvious contamination with elements heavier than silicon. NRA was used to quantify
38
39
40 oxygen and check the carbon content (Figure S1). The evolution of composition assessed from
41
42
43 integration of the RBS and NRA signals is illustrated in Table 1. For the as-grown film, the RE to
44
45
46 oxygen ratio is close to the expected stoichiometric value (0.4) but with a slight excess of oxygen.
47
48
49
50
51 This excess is likely due to the diffusion of oxygen inside the sesquioxide structure during the
52
53
54 annealing under air. Another source of oxygen over-stoichiometry is the formation of silicate
55
56
57
58
59
60

1
2
3 parasitic phases at the silicon interface during the pre-annealing of the Y_2O_3/Si template prior to
4
5
6 Eu_2O_3 deposition. Using SIMNRA software fitting, we evaluate a SiO_2 layer of 30 nm for a 900°C
7
8
9
10 annealing post treatment, in reasonably good agreement with the 22 nm determined by
11
12
13 spectroscopic ellipsometry (Figure S2). When the annealing temperature of the multilayer is
14
15
16 increased above 900 °C, interfacial reactions take place again leading to a further increase of the
17
18
19 oxygen content (see Table 1). An increase of the SiO_2 interlayer's thickness was evidenced by
20
21
22 spectroscopic ellipsometry measurements (Figure S2) and is reported in the last column of Table
23
24
25
26 1. The silicon oxidation is also clearly evidenced on the RBS spectra of Fig. 2c where a shoulder
27
28
29 at the silicon edge appears, indicating the formation of an oxide interlayer. Annealing at
30
31
32 temperatures higher than 1000 °C could not be carried out since the reaction between the layer
33
34
35 and the substrate leads to a depletion of the 120 nm-thick yttria layer into orthosilicate and/or
36
37
38 pyrosilicate phases, which are not desirable.^{14,26} This indeed sets the upper temperature limit for
39
40
41 annealing such multilayers if one wants to keep a constant crystalline environment for the ions.
42
43
44
45
46
47
48
49
50
51
52
53
54
55
56
57
58
59
60

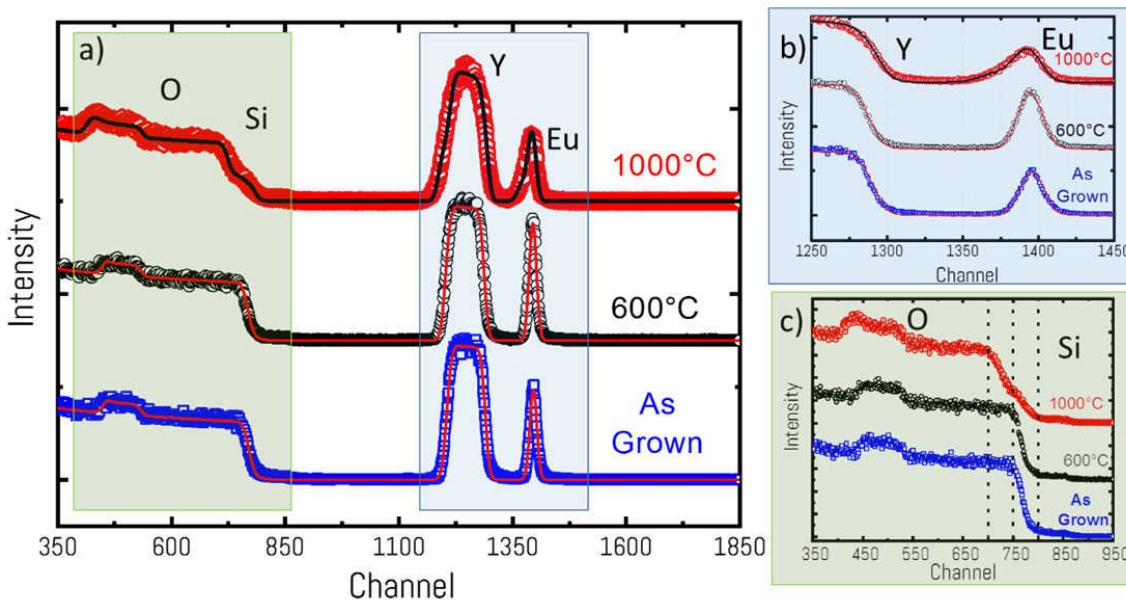


Figure 2 (a) RBS spectra of a $\text{Eu}_2\text{O}_3/\text{Y}_2\text{O}_3/\text{Si}$ stack either as-grown or annealed at 600 or 1000 °C for 2 h. (b) Zoom into the region highlighted in blue. Experimental data are dots points whereas SIMNRA simulation is presented with solid lines. (c) Zoom into the region highlighted in green. Data are vertically translated for better clarity.

Table 1: RBS and NRA quantification data. The SiO_2 thickness estimated from ellipsometry is also presented. The oxygen content used for the determination of the integrated stoichiometry was determined by subtracting the oxygen content in the parasitic interfacial layers determined

1
2
3
4 by the RBS simulation to the total content of oxygen. A good agreement between the thickness
5
6
7 of the SiO₂ layer determined by the RBS simulation and ellipsometry is observed. The expected
8
9
10 stoichiometry is 0.4. * Note that for the as-grown layer, pre-annealing of the Y₂O₃ layer at 900 °C
11
12
13 for 2 h was carried out prior to Eu₂O₃ deposition.
14
15
16

Samples	Y RBS (10 ¹⁵ at/cm ²)	Eu RBS (10 ¹⁵ at/cm ²)	O NRA (10 ¹⁵ at/cm ²)	Stoichiometry [(Y+Eu)/ (Y+Eu+O *)	SiO ₂ thickness ellipsometry (nm)
As grown*	301	20	670	0.35	22
600 °C / 2 h	301	24	690	0.35	24
800 °C / 2 h	301	15	702	0.35	28
900 °C / 2 h	296	14	836	0.35	52
950 °C / 2 h	298	24	1071	0.34	107
1000 °C / 2 h	307	21	1081	0.34	118

17
18
19
20
21
22
23
24
25
26
27
28
29
30
31
32
33
34
35
36
37
38
39
40
41
42
43
44
45
46
47
48 We then evaluate europium diffusion into the yttrium oxide layer beneath. Yttrium and europium
49
50
51 have the same valence state (3+) and similar ionic radii (4 % difference) that lead to possible
52
53
54 inter-diffusion when heated.²⁷ RBS spectra of Figure 2a were fitted using the SIMNRA software.
55
56
57
58
59
60

1
2
3 The staircase-shape Eu^{3+} depth profile that was used to get a good fit is presented in Figure 3 for
4
5
6 different annealing temperatures. We observe that the Eu^{3+} distribution starts to change only for
7
8
9 temperatures above 900°C with significant Eu^{3+} and Y^{3+} inter-diffusion at 950°C . This large
10
11
12 temperature of inter-diffusion is due to the refractory character of Y_2O_3 and Eu_2O_3 with melting
13
14
15 temperatures of about 2400°C . We note though that the considered films are polycrystalline and
16
17
18 that higher diffusion is expected than in single crystal materials due to the presence of grain
19
20
21 boundaries. For the 1000°C case, the RBS composition indicates that europium concentration
22
23
24 starts to be depleted at the surface. The concentration distribution after a diffusion anneal is
25
26
27 described by the thin film diffusion solution.²⁸ Therefore, we fit the curve with the diffusion
28
29
30 Gaussian function such as :²⁸
31
32
33

$$34$$
$$35$$
$$36 C(x,t) = A * \exp\left(-\frac{x^2}{4Dt}\right) \text{ with } A = \frac{\tau C_0}{\sqrt{\pi Dt}} \text{ (eq. 2.)}$$
$$37$$
$$38$$
$$39$$
$$40$$

41 where τ is the initial film thickness of Eu_2O_3 , C_0 is the maximum solid solubility of Eu^{3+} in Y_2O_3 .
42
43
44 Using this equation, we were able to simulate the staircase profile considered in our RBS fit (see
45
46
47 blue and red square curves of Fig. 3) and to extract a diffusion coefficient of 4.5×10^{-21} and 2×10^{-20}
48
49
50 $\text{m}^2 \cdot \text{s}^{-1}$ at 950 and 1000°C respectively. However, a relatively large uncertainty is expected due
51
52
53
54
55
56
57
58
59
60

mainly to the low accuracy in depth resolution of RBS and the surface roughness. In order to obtain more precisely the diffusion coefficient, TOF-SIMS analyses were performed.

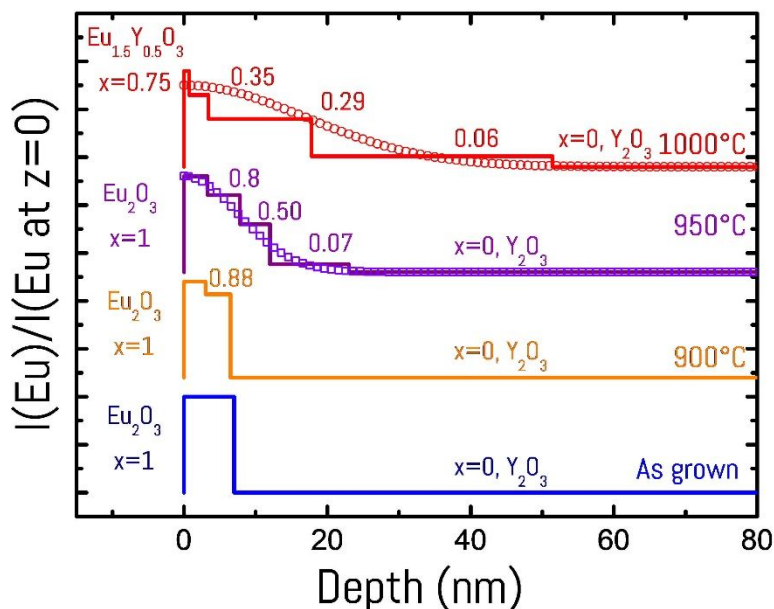


Figure 3. Comparison of diffusion depth profiles of Eu in the $\text{Eu}_2\text{O}_3/\text{Y}_2\text{O}_3/\text{Si}$ stack for different annealing temperatures. The solid lines correspond to the staircase Eu distribution used in the SIMNRA simulation of the RBS spectra. For the two highest temperatures, we simulate the diffusion with the Gaussian function distribution using Eq. 2 (dots and square points). The depth (z) has been determined assuming a density of 5.3 g cm^{-3} and 7.02 g cm^{-3} for Y_2O_3 and Eu_2O_3 respectively. The cationic composition has been indicated for each sublayer using the ratio x

1
2
3 where $x = N_{Eu}/(N_{Eu}+N_Y)$. The data have been vertically shifted and normalized to the Eu content
4
5
6
7 value at the surface ($Z=0$) for clarity.
8
9

10 The main advantage of TOF-SIMS is the sub-nm depth resolution in comparison to the few nm
11
12 resolution of RBS. The depth profiles of Eu, Y, Si, C and O in the as-grown thin layers are
13
14 presented in Fig. 4. Carbon contamination is clearly detected which is expected to originate mainly
15
16 from the surface and possibly from the long carbon chains of the ALD precursors. The TOF SIMS
17
18 spectra demonstrated a chemically stable and well-defined interface between Eu_2O_3 , Y_2O_3 and Si
19
20 for the as-grown layers from the abrupt changes and little overlapping of the signals. Eu ions
21
22 appear to be located within the top 15 nm. When the sample is annealed at high temperature, the
23
24 Eu signal spread out over up to 60 nm (Fig. 4b and 4c) confirming diffusion. Using the same
25
26 equation as before (Eq. 2), we were able to estimate the diffusion coefficients to 4×10^{-21} and
27
28 $1.8 \times 10^{-20} \text{ m}^2 \cdot \text{s}^{-1}$ at 950°C and 1000°C respectively. The results plotted in Fig. 5 together with
29
30 those estimated by RBS indeed agree fairly well.
31
32
33
34
35
36
37
38
39
40
41
42
43
44
45
46
47
48
49
50
51
52
53
54
55
56
57
58
59
60

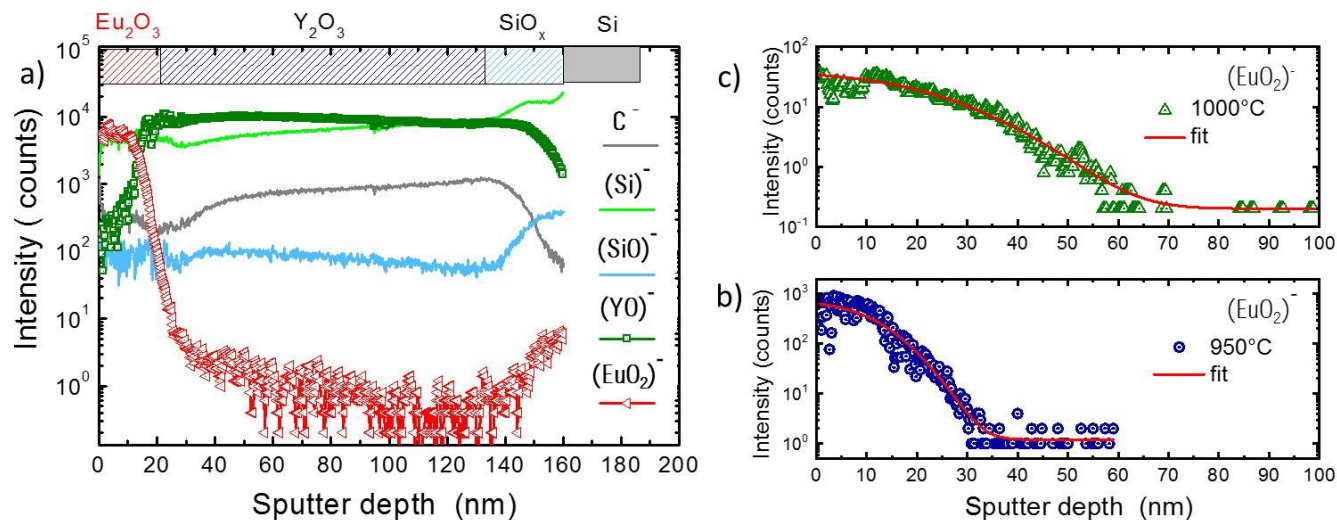
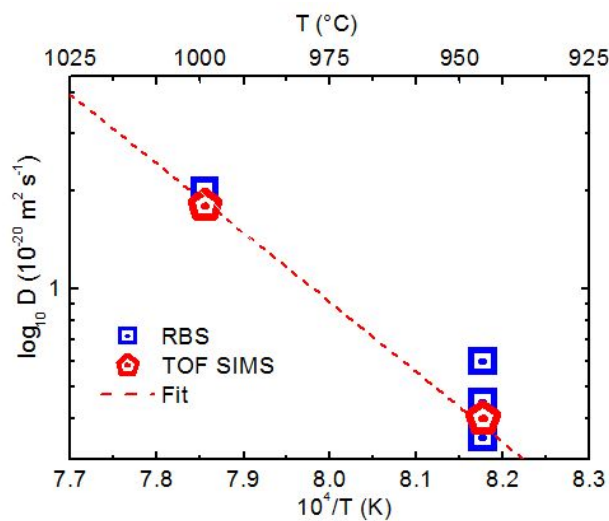


Figure 4: TOF-SIMS analysis of a thin $\text{Eu}_2\text{O}_3/\text{Y}_2\text{O}_3/\text{Si}$ stack. (a) Before annealing from which the different layers can be clearly identified. (b) and (c) Profiles of the Eu element for annealing at 1000 °C and 950°C for 2h. Dots are experimental results while solid lines are modelling using diffusion equations (eq. 2).



1
2
3 *Figure 5: Europium's diffusion coefficient as a function of the reciprocal of the absolute*
4 *annealing temperature (Arrhenius plot) from TOF SIMS and RBS. Symbols are experimental*
5
6 *points and solid line is the fit using an Arrhenius law. For 950°C annealing post-treatment*
7
8 *measurements have been performed for different durations.*
9
10
11
12
13
14
15
16

17 From those measurements, we deduced the activation energy according to the well-known
18
19 Arrhenius equation:
20
21

$$22 \quad D(T) = D_0 e^{-\left(\frac{E_a}{RT}\right)} \quad (\text{eq. 3})$$

23
24
25
26
27
28

29 where D_0 is a prefactor, E_a is the activation energy and T the temperature. The activation energy
30
31 is about 249 kJ mol⁻¹ for both RBS and SIMS data. As only two temperatures have been
32
33 considered, this calculation has limited validity. Nevertheless, those E_a values are close to those
34
35 of self-diffusion reported for yttrium in the literature that are comprised between 246 and 320 kJ
36
37 mol⁻¹ for higher temperature treatments in a Y₂O₃ single crystal.²⁹
38
39
40
41
42
43
44
45

46 In summary, Eu³⁺-diffusion into a polycrystalline ALD film of Y₂O₃ occurs significantly only
47
48 for temperatures above 900 °C, while the formation of an interfacial oxide phase on silicon
49
50 remains limited in the 900°C-1000°C annealing temperature range. This indicates that post-
51
52
53
54
55
56
57
58
59
60

1
2
3 deposition thermal treatment at moderate temperatures can be harnessed to improve the
4
5
6 luminescent properties of ALD-grown films without affecting the in-depth spatial localization of RE
7
8
9 ions. This approach opens the way to the fabrication of complex planar multilayer structures in
10
11
12 order to increase the photoluminescence or to manage energy transfer using the same strategies
13
14
15 than that used with multi core-shell doping in up-conversion nanocrystals.³⁰⁻³² We then extended
16
17
18 this approach to the context of QTs where localized emitters closed to the surface are especially
19
20
21 desirable. For that purpose, we probed Eu^{3+} ion diffusion into quantum-grade quality Y_2SiO_5 single
22
23
24 crystals since YSO has already been used in some of the most advanced demonstrations in
25
26
27
28
29 QTs.³³⁻³⁵
30
31
32

33 3.2. Eu^{3+} diffusion in Y_2SiO_5 single crystals

34
35
36

37 A 20 nm-thick Eu_2O_3 ALD film was deposited on undoped Y_2SiO_5 single crystal substrates that
38
39
40 were cut perpendicular to the *b* axis and optically polished (Fig. 1b). Different annealing
41
42
43 temperatures and duration times, as shown in Table 2, were used to activate diffusion from the
44
45
46 Eu^{3+} containing layer into the crystal. Analysis was carried out by a combination of TOF-SIMS
47
48
49 and RBS. In the RBS spectra of Figure 6, the calculated Eu^{3+} atomic density from the integration
50
51
52 of the peak appears constant and independent of the thermal post-treatment (see Table S1)
53
54
55
56
57
58
59
60

1
2
3 indicating that Eu^{3+} loss does not occur. However, with annealing at temperatures above 1200 °C,
4
5
6 the RBS Eu^{3+} -related peak became asymmetric on the low energy side (i.e. at greater depths)
7
8
9 confirming Eu^{3+} diffusion into the YSO substrate. Moreover, a Y out-diffusion into the film is also
10
11
12 observed since the Y-related contribution of the substrate becomes modified on the high-energy
13
14
15 side (i.e. indicating Y atoms are located closer to the surface). Apart from this, no modification of
16
17
18 the substrate was observed even for the highest annealing temperatures. This is a clear
19
20
21 advantage of this approach as compared to the previously considered thin ALD multilayer stack
22
23
24 where the formation of an interlayer oxide with the substrate limits the maximum annealing
25
26
27 temperature. To evaluate diffusion from the film, we performed simulation of the RBS spectra with
28
29
30 SIMNRA multilayer. However due to the low depth resolution and the overlapping of the 2 main
31
32
33 peaks (Y and Eu) a precise value of the diffusion coefficient could not be extracted. We thus
34
35
36 turned to TOF-SIMS that can provide more accurate depth analysis.
37
38
39
40
41
42
43
44
45
46
47
48
49
50
51
52
53
54
55
56
57
58
59
60

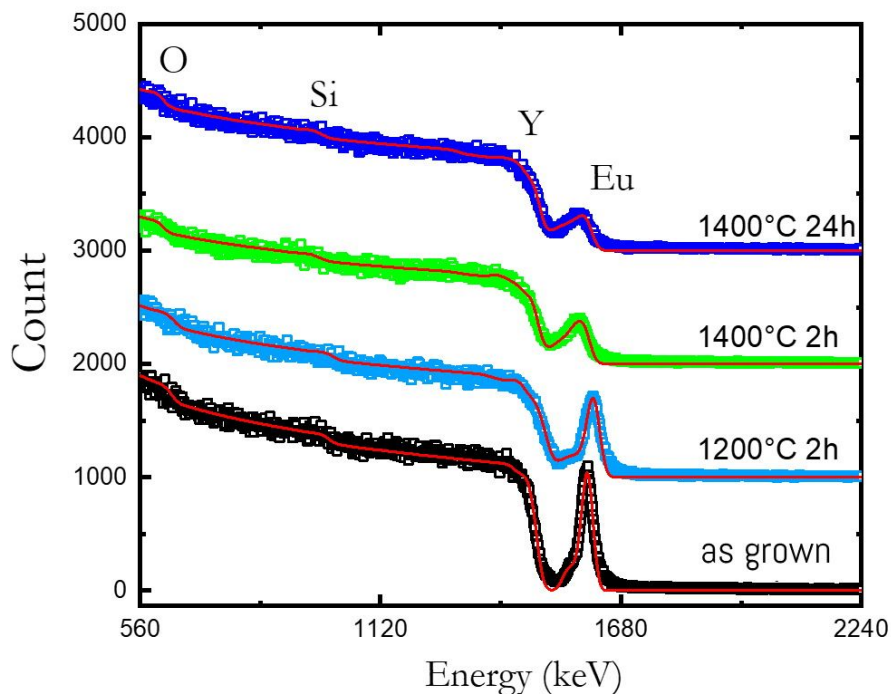


Figure 6: RBS spectra showing europium diffusion from a Eu_2O_3 ALD layer into a Y_2SiO_5 single crystal substrate as a function of the annealing treatment. Square points are experimental data whereas solid lines represent simulation with the SIMNRA software. For all curves, a similar content of europium has been deduced from the simulation (see Table S1). The curves have been translated vertically for better clarity.

Typical experimental curves relative to Eu and Y contributions in TOF-SIMS are presented in Fig.

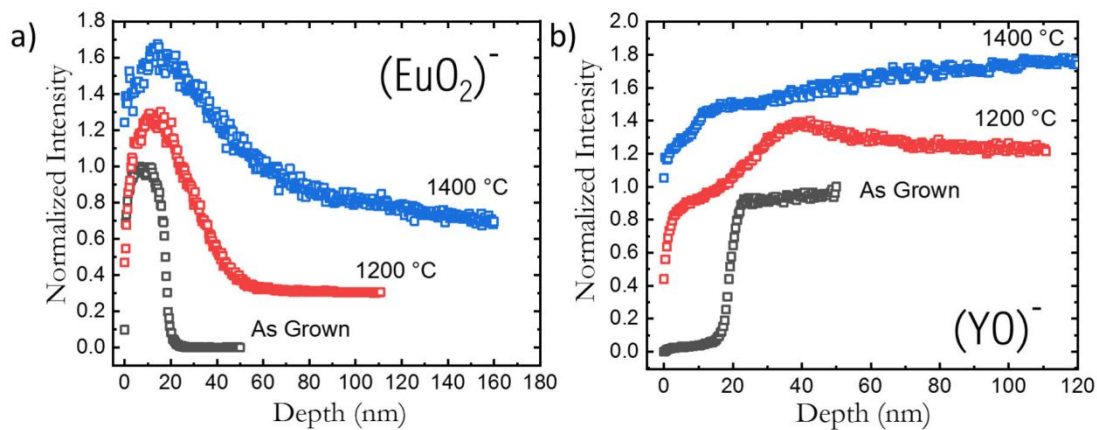
7. For the as-grown ALD film, an abrupt decrease of the EuO_2^- signal indicates a well-defined interface between the 20 nm-thick Eu_2O_3 film and the YSO substrate. When the annealing temperature is increased up to 1400 °C, diffusion of Eu ions into YSO occurs as shown from the

1
2
3 spreading of the EuO_2^- signal (Fig. 7a). Similarly, diffusion of yttrium ions from the substrate into
4
5
6 the ALD layer is also visible from the shape of the YO^- signal in Fig. 7b. When looking in more
7
8
9 details at the Eu-related contribution, one can note that for short annealing, the semi-logarithmic
10
11
12 plot indicates a two-component concentration profile of Eu inside YSO, which is far less observed
13
14
15 for the long 1400°C annealing (see Fig. 8a and 8b). In the latter case, Eu^{3+} distribution can be
16
17
18 well fitted by a Gaussian distribution (Eq. 2). Two-component diffusion profiles have already been
19
20
21 observed in polycrystalline materials such as ceramics and have been classified by Harrison in
22
23
24 three different kinetics regimes called A, B and C.^{28,36} These different regimes exist due to the
25
26
27 presence of several diffusion paths with different coefficients. Indeed, the diffusion coefficient
28
29
30 inside the bulk material is significantly smaller than at the grain boundary for polycrystalline
31
32
33 materials or for diffusion at dislocations in single crystals. For the A regime the bulk diffusion and
34
35
36 the faster diffusion process are averaged and only an effective diffusion D_{eff} coefficient is
37
38
39 observed. This A kinetics is observed for high temperature or longer annealing times and a
40
41
42 Gaussian diffusion profile is expected for depleted source. For the B regime, the diffusion profile
43
44
45 presents two different slopes. The first slope of the profile corresponds to the effective diffusion
46
47
48 D_{eff} across the bulk materials whereas the second part of the profile, i.e. the curved tail, is
49
50
51 characteristic of the diffusion along the fast path (grain boundaries, dislocation etc...).²⁸ Indeed,
52
53
54
55
56
57
58
59
60

1
2
3 thermal diffusion of ions in single crystals has revealed that large tails in the concentration profile
4
5
6 can be created as a consequence of the existence of dislocations that act as “short circuits” for
7
8
9 the thermally diffused ions, leading to unusually large penetration.³⁷ The C kinetics corresponds
10
11
12 to condition where bulk diffusion is extremely low and is not in agreement with our experimental
13
14
15 conditions. According to Harrison model only one diffusion is expected in single crystal but the B
16
17
18 regime has already been observed in several materials.^{37,38} Possible explanations are the
19
20
21 existence of dislocations or of large anisotropy cationic diffusion with the direction as already
22
23
24 observed for other oxide.^{25,38} The latter effect should be important in our crystal since YSO is
25
26
27 monoclinic. Indeed, for YSO the diffusion parameter is described with a second rank symmetric
28
29
30 tensor with 4 independent parameters. More studies are required in order to fully characterize this
31
32
33 process.
34
35
36
37
38

39 The diffusion coefficients extracted from the Gaussian distribution for different temperatures or
40
41
42 annealing durations are presented in Table 2. As expected, an increase of the diffusion
43
44
45 coefficients is observed with the annealing temperature. For example for two hours annealing,
46
47
48 the effective diffusion coefficient is estimated to 2×10^{-21} and $10 \times 10^{-20} \text{ m}^2 \cdot \text{s}^{-1}$ at 1200 and 1400 °C
49
50
51 respectively. The obtained diffusion coefficients of Eu^{3+} in YSO are of the same order of
52
53
54 magnitude than in other oxide materials (such as YVO_4 and YAG) that were shown for comparison
55
56
57
58
59
60

1
2
3 in Table 2. Finally, the calculated diffusion coefficients were plotted in Fig. 9 as a function of
4
5
6 temperature. The activation energy of Eu^{3+} in YSO was estimated to $260 \text{ kJ}\cdot\text{mol}^{-1}$. This value is
7
8
9 in the characteristic range for lanthanides in oxide single crystals.²⁰
10
11
12
13



14
15
16
17
18
19
20
21
22
23
24
25
26
27
28
29
30
31 *Figure 7: TOF-SIMS analysis of a thin ALD-grown Eu_2O_3 thin film on Y_2SiO_5 showing the Eu and*
32
33
34 *Y related signals at different annealing temperatures. Annealing duration was 2 h. The curves*
35
36
37 *have been normalized to their maximum and vertically translated for better clarity.*
38
39
40
41
42
43
44
45
46
47
48
49
50
51
52
53
54
55
56
57
58
59
60

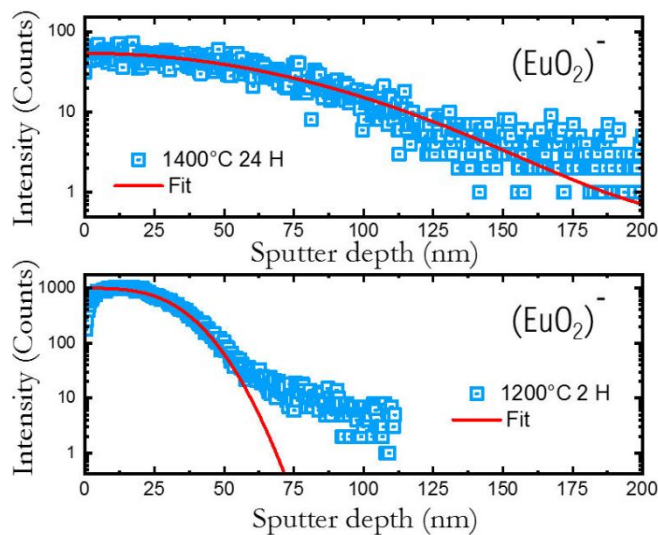


Figure 8: Higher resolution Eu-related TOF-SIMS signals of a thin ALD-grown Eu_2O_3 thin film on Y_2SiO_5 for annealing at $1200\text{ }^\circ\text{C}$ for 2h and $1400\text{ }^\circ\text{C}$ for 24 h. Dots are experimental data while solid lines are modelling using the diffusion equation (Eq. 2). One can note that a two-component contribution is visible for the $1200\text{ }^\circ\text{C}$ annealing sample.

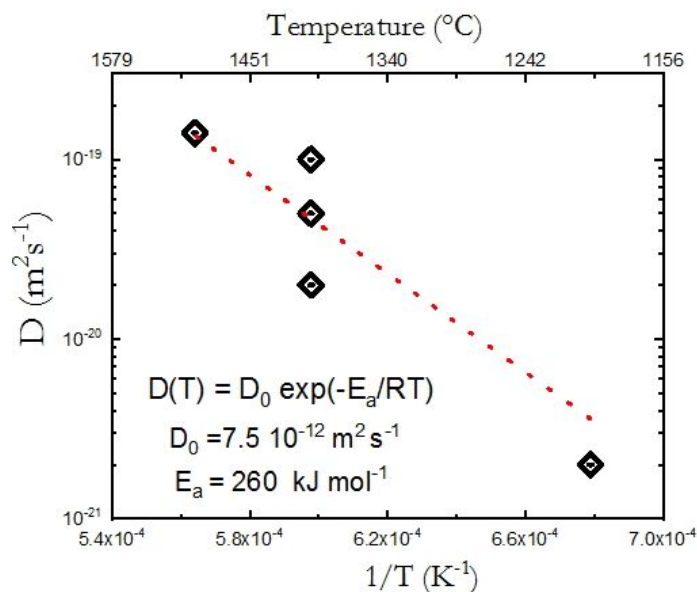


Figure 9: Arrhenius plot for Eu^{3+} diffusion in single crystal Y_2SiO_5 from TOF-SIMS measurements.

The line is a least-squares fit of the data. Arrhenius parameters extracted from the fit are presented in the figure.

Table 2: Diffusion parameters and measured diffusion coefficients. Example from the literature have been added for comparison.

Crystal	Doping element	Annealing Temperature (°C)	Annealing Time (Hours)	D ($\times 10^{-20} \text{ m}^2 \text{ s}^{-1}$)	REF
Y_2SiO_5	Eu^{3+}	1200	2	0.2	This work
Y_2SiO_5	Eu^{3+}	1400	2	10	This work
Y_2SiO_5	Eu^{3+}	1400	10	5.0	This work
Y_2SiO_5	Eu^{3+}	1400	24	2.2	This work
Y_2SiO_5	Eu^{3+}	1500	2	13.4	This work
YVO_4	Nd^{3+}	1400	24	78	19
$\text{Y}_3\text{Al}_5\text{O}_{12}$	Nd^{3+}	1200	25	0.26	17
$\text{Y}_3\text{Al}_5\text{O}_{12}$	Yb^{3+}	1450	24.1	4.3	39,40
Al_2O_3	Tr^{3+}	1200	48	3	41

3.3. Optical properties of in-diffused europium ions

Eventually, we evaluated the optical properties of Eu^{3+} ions diffused from the ALD layer into the YSO substrate. To this end, spectral hole burning (SHB) experiments were performed in fluorescence detection mode on a sample annealed for 90 h at 1400°C (more information is available in the supporting information file). SHB is a highly sensitive technique used to probe the material's crystalline quality.^{42,43} In this process, population is transferred from the ground state through the excited state of interest to metastable states : the hyperfine levels (see Figure S6). Indeed, dopant properties, such as optical linewidth or nuclear spin lifetime, are strongly affected by crystal disorder (e.g. stacking fault, vacancies, mechanical strain, electric and magnetic noise). Moreover, the width of the spectral hole can provide information on the optical coherence lifetime since in the absence of power or laser broadening; it is expected to be twice the effective homogeneous linewidth. This linewidth is extremely sensitive to dynamical perturbation (moving charges, spin flip flop, two level systems) and acts as an extremely sensitive strain and disorder probe and so SHB appears as a useful method to probe the surface.⁴² We used several high intensity burning pulses at a given frequency to resonantly excite the Eu^{3+} ions into their $^5\text{D}_0$ state and create a corresponding transparency window in the inhomogeneously broadened absorption line (for more detail see

1
2
3 Figure S5 and S6). Then after a delay of a few ms in order for the Eu^{3+} fluorescence to vanish, a
4
5
6 subsequent weaker laser pulse (probe laser) was sent to the sample. This probe pulse was
7
8
9 frequency swept across the burned hole frequency (-20 MHz, +20 MHz), with an acousto-optic
10
11
12 modulator (AOM) to measure the excitation spectrum. Indeed in order to probe the pulse we
13
14
15 worked in excitation mode by probing the change in the area of the red emission (i.e. the ${}^5\text{D}_0 \rightarrow$
16
17
18 ${}^7\text{F}_2$ transition) as a function of the probe pulse wavelength. This change is due to the increased
19
20
21 transparency at the hole position. First, we calibrated the experimental setup by burning a hole in
22
23
24 a low Eu^{3+} -doped bulk Y_2SiO_5 single crystal (Figure S7). This measurement is useful in order to
25
26
27 estimate the additional broadening induced by the experimental conditions such as temperature,
28
29
30 power broadening, laser linewidth and also laser stability. SHB signals recorded with this
31
32
33 sequence present a hole FWHM of about 1.7 MHz (Figure S7). This value is broader than the
34
35
36 best values reported for $\text{Eu}^{3+}:\text{YSO}$ typically in the kHz range.^{44–46} In our experiment an additional
37
38
39 experimental broadening arises from the linewidth of our laser (300 kHz), the laser instability and
40
41
42 the power broadening from this strongly focused configuration. SHB data was then recorded on
43
44
45 the in-diffused sample (Fig. 10) for which the europium diffusion length ($2\sqrt{Dt}$) is estimated to
46
47
48 200 nm. To select the emission contribution originating from the in-diffused ions at the surface,
49
50
51 we first aligned the setup in order to maximize the laser reflection at the surface. Then, a spectral
52
53
54
55
56
57
58
59
60

1
2
3 hole was burned at the central frequency of 580.041 nm, from which, a promising hole linewidth
4
5
6 as narrow as 4 MHz was obtained. This is about twice that of the low Eu^{3+} doped bulk reference
7
8
9 sample. This difference is likely related to the higher Eu concentration at the surface (Figure 8).

10
11
12 To discard any contribution from trace Eu^{3+} ions in the YSO substrate also absorbing at the same
13
14
15 central frequency, a second SHB experiment was performed at a slightly different wavelength of
16
17
18 580.057 nm, which is 15 GHz away from the central position of the inhomogeneous line.
19
20
21

22
23 According to a study on an Eu^{3+} :YSO single crystal grown by crystal pulling, the inhomogeneous
24
25 linewidth is expected to linearly increase with Eu^{3+} concentration of about 21 GHz/%.⁴⁷ This
26
27
28 concentration dependency suggest that the second SHB experiment is performed on Eu^{3+} ions
29
30
31 closer to the surface. At this wavelength a hole can still be burned but with a larger FWHM (6
32
33
34 MHz) and shallower depth than the previous one. One possibility to explain the larger broadening
35
36
37 in the diffused area compared to the reference, could be that an increase in concentration leads
38
39
40 to some disorder in the structure that generates additional dynamical dephasing processes like
41
42
43 Two Level System (TLS).¹⁶ This disorder arises from possible variations of the local stoichiometry
44
45
46 or interstitial defects since cation exchange occurs between two different material, Eu_2O_3 and
47
48
49 Y_2SiO_5 respectively. More high-resolution spectroscopy measurements are required to determine
50
51
52 the predominant dephasing mechanism. Anyway, this work demonstrates that RE ions can be
53
54
55
56
57
58
59
60

spatially localized near the surface by a two-step process based on ALD deposition and annealing

post-treatment under appropriate conditions, while retaining their excellent optical properties.

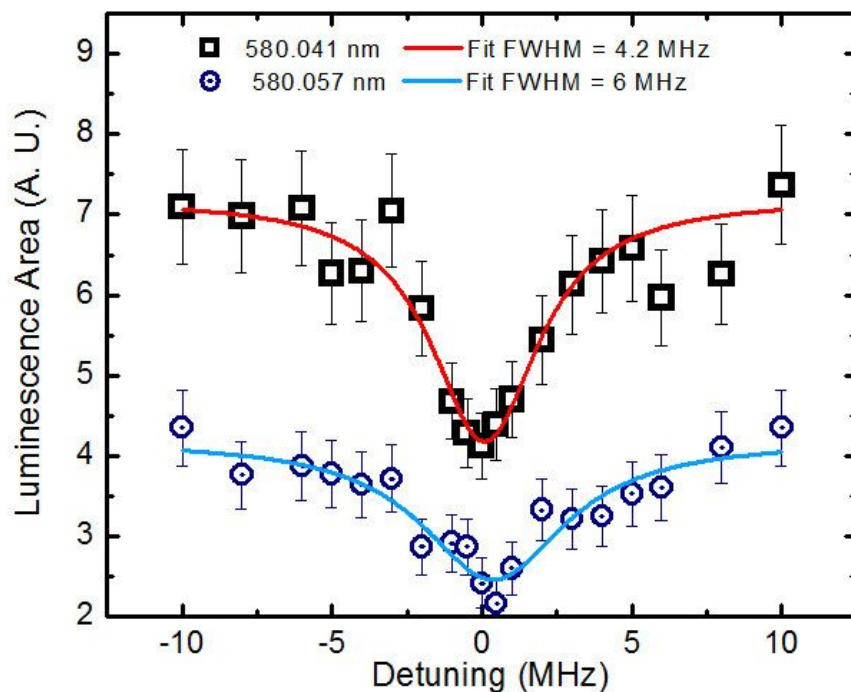


Figure 10. Fluorescence-detection of spectral holes burned on an ALD- Eu_2O_3 thin film on Y_2SiO_5 annealed 90 h at 1400°C . Measurements at two different wavelengths of the inhomogeneous line are presented and the linewidth is given. Curves are vertically translated for better clarity.

Conclusion

In this work, we studied the ability of the ALD technique to spatially localize rare-earth ion emitters with good optical properties. In particular, we evaluated Eu^{3+} ion diffusion from few nanometers-

1
2
3 thin Eu_2O_3 film grown by ALD into a polycrystalline Y_2O_3 film or into a single crystal Y_2SiO_5
4
5
6 substrate after thermal annealing in the 900-1400 °C range. While such high temperature post-
7
8
9 treatments are essential to improve the crystallinity of thin ALD films, they lead to a partial loss of
10
11
12 RE ion localization. On the other hand, this behavior can be harnessed to locally diffuse emitters
13
14
15 in the close proximity of the crystal surface.
16
17
18
19

20
21 Based on RBS and TOF-SIMS analyses, we observed that Eu^{3+} diffusion into polycrystalline
22
23 Y_2O_3 becomes effective at lower temperatures (900 °C) in comparison to single crystal YSO
24
25
26 (1200 °C). This is attributed to the presence of grain boundaries that increase diffusion kinetics.
27
28
29 Diffusion coefficients of about 4×10^{-21} and $2 \times 10^{-20} \text{ m}^2 \cdot \text{s}^{-1}$ at 950 and 1000 °C respectively in poly-
30
31
32 Y_2O_3 and 2×10^{-21} and $10 \times 10^{-20} \text{ m}^2 \cdot \text{s}^{-1}$ at 1200 and 1400 °C respectively were measured in a YSO
33
34
35 single crystal.
36
37
38
39

40
41 This investigation indicates that, based on the nanometer-scale deposition ability of ALD
42
43
44 associated with an appropriate thermal annealing, rare-earth oxide materials can be engineered
45
46
47 with specific nanostructures in which dopant localization is well controlled. We eventually
48
49
50 demonstrate that excellent optical properties are retained for such in-diffused near-surface RE
51
52
53 ions in YSO. Spectral hole burning showed values as low as 4 MHz which could be improved by
54
55
56
57
58
59
60

1
2
3 changing the composition of the top Eu_2O_3 layer that may lead to too high Eu^{3+} concentration in
4
5
6 the vicinity of the surface. This approach could provide an attractive alternative to rare-earth ion
7
8
9 implantation and will be further explored in QTs applications such as quantum memories and
10
11
12 quantum sensors. Finally, this cation exchange method is versatile and can be applied to a large
13
14
15 range of materials and doping elements (e.g. transition metal).
16
17
18

19 20 **Acknowledgements:**

21
22
23
24 We acknowledge the French EMIR-A network for provision of irradiation beam time using the
25
26
27 SAFIR facility. Région Ile de France is acknowledged for partial funding of the ToF-SIMS
28
29
30 equipment. This project has received funding from the European Union Horizon 2020 research
31
32
33 and innovation program under grant agreement no. 820391 (SQUARE) and no. 712721
34
35
36 (NANOQTECH).
37
38
39
40

41 **References**

- 42
43
44
45
46 (1) Goldner, P.; Ferrier, A.; Guillot-Noël, O. Rare Earth-Doped Crystals for Quantum
47
48 Information Processing. In *Handbook on the Physics and Chemistry of Rare Earths*;
49
50 Bünzli, J.-C. G., Pecharsky, V. K., Eds.; Elsevier, North Holland: Amsterdam, 2015; Vol.
51
52 46, pp 1–78.
53
54 (2) Dibos, A. M.; Raha, M.; Phenicie, C. M.; Thompson, J. D. Atomic Source of Single
55
56 Photons in the Telecom Band. *Phys. Rev. Lett.* **2018**, *120* (24), 243601.
57
58 <https://doi.org/10.1103/PhysRevLett.120.243601>.
59
60

- 1
2
3
4 (3) Zhong, T.; Kindem, J. M.; Bartholomew, J. G.; Rochman, J.; Craiciu, I.; Miyazono, E.;
5 Bettinelli, M.; Cavalli, E.; Verma, V.; Nam, S. W.; Marsili, F.; Shaw, M. D.; Beyer, A. D.;
6 Faraon, A. Nanophotonic Rare-Earth Quantum Memory with Optically Controlled
7 Retrieval. *Science* **2017**, *357*(6358), 1392–1395.
8 <https://doi.org/10.1126/science.aan5959>.
9
10
11 (4) Tielrooij, K. J.; Orona, L.; Ferrier, A.; Badioli, M.; Navickaite, G.; Coop, S.; Nanot, S.;
12 Kalinic, B.; Cesca, T.; Gaudreau, L.; Ma, Q.; Centeno, A.; Pesquera, A.; Zurutuza, A.; de
13 Riedmatten, H.; Goldner, P.; García de Abajo, F. J.; Jarillo-Herrero, P.; Koppens, F. H. L.
14 Electrical Control of Optical Emitter Relaxation Pathways Enabled by Graphene. *Nat.*
15 *Phys.* **2015**, *11*(3), 281–287. <https://doi.org/10.1038/nphys3204>.
16
17 (5) Casabone, B.; Benedikter, J.; Hümmer, T.; Oehl, F.; Lima, K. de O.; Hänsch, T. W.;
18 Ferrier, A.; Goldner, P.; Riedmatten, H. de; Hunger, D. Cavity-Enhanced Spectroscopy of
19 a Few-Ion Ensemble in $\text{Eu}^{3+}:\text{Y}_2\text{O}_3$. *New J. Phys.* **2018**, *20*(9), 095006.
20 <https://doi.org/10.1088/1367-2630/aadf68>.
21
22 (6) Wolf, T.; Neumann, P.; Nakamura, K.; Sumiya, H.; Ohshima, T.; Isoya, J.; Wrachtrup, J.
23 Subpicotesla Diamond Magnetometry. *Phys. Rev. X* **2015**, *5*(4), 041001.
24 <https://doi.org/10.1103/PhysRevX.5.041001>.
25
26 (7) Hoang, J.; Schwartz, R. N.; Wang, K. L.; Chang, J. P. Er^{3+} Interlayer Energy Migration as
27 the Limiting Photoluminescence Quenching Factor in Nanostructured $\text{Er}^{3+}:\text{Y}_2\text{O}_3$ Thin
28 Films. *J. Appl. Phys.* **2012**, *112*(2), 023116. <https://doi.org/10.1063/1.4737793>.
29
30 (8) Groot-Berning, K.; Kornher, T.; Jacob, G.; Stopp, F.; Dawkins, S. T.; Kolesov, R.;
31 Wrachtrup, J.; Singer, K.; Schmidt-Kaler, F. Deterministic Single-Ion Implantation of Rare-
32 Earth Ions for Nanometer-Resolution Color-Center Generation. *Phys. Rev. Lett.* **2019**,
33 *123*(10), 106802. <https://doi.org/10.1103/PhysRevLett.123.106802>.
34
35 (9) van Dam, S. B.; Walsh, M.; Degen, M. J.; Bersin, E.; Mouradian, S. L.; Galiullin, A.; Ruf,
36 M.; IJspeert, M.; Taminiau, T. H.; Hanson, R.; Englund, D. R. Optical Coherence of
37 Diamond Nitrogen-Vacancy Centers Formed by Ion Implantation and Annealing. *Phys.*
38 *Rev. B* **2019**, *99*(16), 161203. <https://doi.org/10.1103/PhysRevB.99.161203>.
39
40 (10) Kukharchyk, N.; Shvarkov, S.; Probst, S.; Xia, K.; Becker, H.-W.; Pal, S.; Markmann, S.;
41 Kolesov, R.; Siyushev, P.; Wrachtrup, J.; Ludwig, A.; Ustinov, A. V.; Wieck, A. D.;
42 Bushev, P. Nanoscale Nonlinear Effects in Erbium-Implanted Yttrium Orthosilicate. *J.*
43 *Lumin.* **2016**, *177*, 266–274. <https://doi.org/10.1016/j.jlumin.2016.05.010>.
44
45
46
47
48
49
50
51
52
53
54
55
56
57
58
59
60

- 1
2
3
4 (11) Kolesov, R.; Xia, K.; Reuter, R.; Stöhr, R.; Zappe, A.; Meijer, J.; Hemmer, P. R.;
5 Wrachtrup, J. Optical Detection of a Single Rare-Earth Ion in a Crystal. *Nat. Commun.*
6 **2012**, *3*(1), 1029. <https://doi.org/10.1038/ncomms2034>.
7
8 (12) Proslie, T.; Becker, N. G.; Pellin, M. J.; Klug, J.; Elam, J. W. Controlling the Emissive
9 Properties of Materials-Improved Lasers and Upconversion Materials. US8518179B1,
10 August 27, 2013.
11
12 (13) Rönn, J.; Karvonen, L.; Kauppinen, C.; Perros, A. P.; Peyghambarian, N.; Lipsanen, H.;
13 Säynätjoki, A.; Sun, Z. Atomic Layer Engineering of Er-Ion Distribution in Highly Doped
14 Er:Al₂O₃ for Photoluminescence Enhancement. *ACS Photonics* **2016**, *3*(11), 2040–
15 2048. <https://doi.org/10.1021/acsp Photonics.6b00283>.
16
17 (14) Scarafagio, M.; Tallaire, A.; Tielrooij, K.-J.; Cano, D.; Grishin, A.; Chavanne, M.-H.;
18 Koppens, F. H. L.; Ringuédé, A.; Cassir, M.; Serrano, D.; Goldner, P.; Ferrier, A. Ultrathin
19 Eu- and Er-Doped Y₂O₃ Films with Optimized Optical Properties for Quantum
20 Technologies. *J. Phys. Chem. C* **2019**, *123*(21), 13354–13364.
21 <https://doi.org/10.1021/acs.jpcc.9b02597>.
22
23 (15) Welinski, S.; Thiel, C. W.; Dajczgewand, J.; Ferrier, A.; Cone, R. L.; Macfarlane, R. M.;
24 Chanelière, T.; Louchet-Chauvet, A.; Goldner, P. Effects of Disorder on Optical and
25 Electron Spin Linewidths in Er³⁺, Sc³⁺:Y₂SiO₅. *Opt. Mater.* **2017**, *63*, 69–75.
26 <https://doi.org/10.1016/j.optmat.2016.09.039>.
27
28 (16) Flinn, G. P.; Ganem, J.; Jones, M. L.; Meltzer, R. S.; Macfarlane, R. M. Sample
29 Dependant Optical Dephasing in Bulk Crystalline Samples of Y₂O₃:Eu. *Phys. Rev. B*
30 **1994**, *49*, 5821.
31
32 (17) Cherniak, D. J. Rare Earth Element and Gallium Diffusion in Yttrium Aluminum Garnet.
33 *Phys. Chem. Miner.* **1998**, *26*(2), 156–163. <https://doi.org/10.1007/s002690050172>.
34
35 (18) Maya, E. G.; Maya, F.; Lesage, B.; LoudjanP, M. I.; Grattapainc, C. Yttrium Diffusion in A-
36 Alumina Single Crystal. 4.
37
38 (19) Hettrick, S. J.; Wilinson, S.; Sheperd, D. P. Neodymium and Gadolinium Diffusion in
39 Yttrium Vanadate. *J. Opt. Soc. Am. B* **2002**, *19*(1), 33.
40
41 (20) Brady, J. B.; Cherniak, D. J. Diffusion in Minerals: An Overview of Published
42 Experimental Diffusion Data. *Rev. Mineral. Geochem.* **2010**, *72*(1), 899–920.
43 <https://doi.org/10.2138/rmg.2010.72.20>.
44
45
46
47
48
49
50
51
52
53
54
55
56
57
58
59
60

- 1
2
3
4 (21) Fujioka, K.; Sugiyama, A.; Fujimoto, Y.; Kawanaka, J.; Miyanaga, N. Ion Diffusion at the
5 Bonding Interface of Undoped YAG/Yb:YAG Composite Ceramics. *Opt. Mater.* **2015**, *46*,
6 542–547. <https://doi.org/10.1016/j.optmat.2015.05.023>.
7
- 8 (22) Schmidt, R. V.; Kaminow, I. P. Metal-Diffused Optical Waveguides in LiNbO₃. *Appl. Phys.*
9 *Lett.* **1974**, *25*, 458.
- 10
11 (23) Wang, T.-J.; Chen, B.-W.; Chen, P.-K.; Chen, C.-H. Er/Si Interdiffusion Effect on
12 Photoluminescent Properties of Erbium Oxide/Silicon Oxide Films Deposited on Silicon.
13 *J. Lumin.* **2017**, *192*, 1065–1071. <https://doi.org/10.1016/j.jlumin.2017.08.050>.
14
15 (24) Ferrier, A.; Tumino, B.; Goldner, Ph. Variations in the Oscillator Strength of the 7 F₀ → 5
16 D₀ Transition in Eu³⁺: Y₂SiO₅ Single Crystals. *J. Lumin.* **2016**, *170*, 406–410.
17 <https://doi.org/10.1016/j.jlumin.2015.07.026>.
18
19 (25) Mayer, M. Improved Physics in SIMNRA 7. *Nucl. Instrum. Methods Phys. Res. Sect. B*
20 *Beam Interact. Mater. At.* **2014**, *332*, 176–180.
21 <https://doi.org/10.1016/j.nimb.2014.02.056>.
22
23 (26) Scarafagio, M.; Tallaire, A.; Chavanne, M.-H.; Cassir, M.; Ringuedé, A.; Serrano, D.;
24 Goldner, P.; Ferrier, A. Improving the Luminescent Properties of Atomic Layer Deposition
25 Eu:Y₂O₃ Thin Films through Optimized Thermal Annealing. *Phys. Status Solidi A* **2020**,
26 1900909. <https://doi.org/10.1002/pssa.201900909>.
27
28 (27) Shannon, R. D.; Prewitt, C. T. Effective Ionic Radii in Oxides and Fluorides. *Acta*
29 *Crystallogr. B* **1969**, *25* (5), 925–946. <https://doi.org/10.1107/S0567740869003220>.
30
31 (28) Mehrer, H. *Diffusion in Solids: Fundamentals, Methods, Materials, Diffusion-Controlled*
32 *Processes*; Springer series in Solid State Science; Springer-Verlag Berlin and Heidelberg
33 GmbH & Co. K, 2009.
34
35 (29) Gaboriaud, R. J. Self-Diffusion of Yttrium in Monocrystalline Yttrium Oxide: Y₂O₃. *J. Solid*
36 *State Chem.* 1980, pp 252–261.
37
38 (30) Zhou, B.; Shi, B.; Jin, D.; Liu, X. Controlling Upconversion Nanocrystals for Emerging
39 Applications. *Nat. Nanotechnol.* **2015**, *10* (11), 924–936.
40 <https://doi.org/10.1038/nnano.2015.251>.
41
42 (31) Wang, F.; Deng, R.; Wang, J.; Wang, Q.; Han, Y.; Zhu, H.; Chen, X.; Liu, X. Tuning
43 Upconversion through Energy Migration in Core–Shell Nanoparticles. *Nat. Mater.* **2011**,
44 *10* (12), 968–973. <https://doi.org/10.1038/nmat3149>.
45
46
47
48
49
50
51
52
53
54
55
56
57
58
59
60

- 1
2
3
4 (32) Wen, S.; Zhou, J.; Zheng, K.; Bednarkiewicz, A.; Liu, X.; Jin, D. Advances in Highly
5 Doped Upconversion Nanoparticles. *Nat. Commun.* **2018**, *9*(1), 1–12.
6 <https://doi.org/10.1038/s41467-018-04813-5>.
7
8 (33) Clausen, C.; Usmani, I.; Bussi eres, F.; Sangouard, N.; Afzelius, M.; Riedmatten, H. de;
9 Gisin, N. Quantum Storage of Photonic Entanglement in a Crystal. *Nature* **2011**, *469*
10 (7331), 508–511. <https://doi.org/10.1038/nature09662>.
11
12 (34) Bussi eres, F.; Clausen, C.; Tiranov, A.; Korzh, B.; Verma, V. B.; Nam, S. W.; Marsili, F.;
13 Ferrier, A.; Goldner, P.; Herrmann, H.; Silberhorn, C.; Sohler, W.; Afzelius, M.; Gisin, N.
14 Quantum Teleportation from a Telecom-Wavelength Photon to a Solid-State Quantum
15 Memory. *Nat. Photonics* **2014**, *8*(10), 775–778.
16 <https://doi.org/10.1038/nphoton.2014.215>.
17
18 (35) Ortu, A.; Tiranov, A.; Welinski, S.; Fr owis, F.; Gisin, N.; Ferrier, A.; Goldner, P.; Afzelius,
19 M. Simultaneous Coherence Enhancement of Optical and Microwave Transitions in Solid-
20 State Electronic Spins. *Nat. Mater.* **2018**, *17*(8), 671–675.
21 <https://doi.org/10.1038/s41563-018-0138-x>.
22
23 (36) Harrison, L. G. Influence of Dislocations on Diffusion Kinetics in Solids with Particular
24 Reference to the Alkali Halides. *Trans. Faraday Soc.* **1961**, *57*, 1191.
25 <https://doi.org/10.1039/tf9615701191>.
26
27 (37) Moya, E. G.; Moya, F.; Sami, A.; Juv e, D.; Tr eheux, D.; Grattepain, C. Diffusion of
28 Chromium in Alumina Single Crystals. *Philos. Mag. A* **1995**, *72*(4), 861–870.
29 <https://doi.org/10.1080/01418619508239939>.
30
31 (38) Sabioni, A. C. S.; Huntz, A. M.; Daniel, A. M. J. M.; Macedo, W. A. A. Measurement of
32 Iron Self-Diffusion in Hematite Single Crystals by Secondary Ion-Mass Spectrometry
33 (SIMS) and Comparison with Cation Self-Diffusion in Corundum-Structure Oxides. *Philos.*
34 *Mag.* **2005**, *85*(31), 3643–3658. <https://doi.org/10.1080/14786430500323795>.
35
36 (39) Marquardt, K.; Ramasse, Q. M.; Kisielowski, C.; Wirth, R. Diffusion in Yttrium Aluminium
37 Garnet at the Nanometer-Scale: Insight into the Effective Grain Boundary Width. *Am.*
38 *Mineral.* **2011**, *96*(10), 1521–1529. <https://doi.org/10.2138/am.2011.3625>.
39
40 (40) Marquardt, K.; Petrishcheva, E.; Abart, R.; Gard es, E.; Wirth, R.; Dohmen, R.; Becker, H.-
41 W.; Heinrich, W. Volume Diffusion of Ytterbium in YAG: Thin-Film Experiments and
42 Combined TEM–RBS Analysis. *Phys. Chem. Miner.* **2010**, *37*(10), 751–760.
43 <https://doi.org/10.1007/s00269-010-0373-4>.
44
45
46
47
48
49
50
51
52
53
54
55
56
57
58
59
60

- 1
2
3
4 (41) Legros, C.; Lesage, B.; Borchardt, G.; Kilo, M.; Jomard, F. Lanthanide Diffusion in Single
5 Crystalline and Polycrystalline Pure or Yttrium Doped Alpha-Alumina. *Defect Diffus.*
6 *Forum* **2005**, *237–240*, 432–437. <https://doi.org/10.4028/www.scientific.net/DDF.237->
7 [240.432](https://doi.org/10.4028/www.scientific.net/DDF.237-240.432).
8
9
10 (42) Bartholomew, J. G.; de Oliveira Lima, K.; Ferrier, A.; Goldner, P. Optical Line Width
11 Broadening Mechanisms at the 10 KHz Level in $\text{Eu}^{3+}:\text{Y}_2\text{O}_3$ Nanoparticles. *Nano Lett.*
12 **2017**, *17*(2), 778–787. <https://doi.org/10.1021/acs.nanolett.6b03949>.
13
14 (43) Lutz, T.; Veissier, L.; Thiel, C. W.; Woodburn, P. J. T.; Cone, R. L.; Barclay, P. E.; Tittel,
15 W. Effects of Fabrication Methods on Spin Relaxation and Crystallite Quality in Tm-
16 Doped $\text{Y}_3\text{Al}_5\text{O}_{12}$ Powders Studied Using Spectral Hole Burning. *Sci. Technol. Adv.*
17 *Mater.* **2016**, *17*(1), 63–70. <https://doi.org/10.1080/14686996.2016.1148528>.
18
19 (44) Oswald, R.; Hansen, M. G.; Wiens, E.; Nevsky, A. Yu.; Schiller, S. Characteristics of
20 Long-Lived Persistent Spectral Holes in
21 $\text{Eu}^{3+}:\text{Y}_2\text{SiO}_5$ at 1.2 K. *Phys. Rev. A* **2018**,
22 *98*(6), 062516. <https://doi.org/10.1103/PhysRevA.98.062516>.
23
24 (45) Gobron, O.; Jung, K.; Galland, N.; Predehl, K.; Le Targat, R.; Ferrier, A.; Goldner, P.;
25 Seidelin, S.; Le Coq, Y. Dispersive Heterodyne Probing Method for Laser Frequency
26 Stabilization Based on Spectral Hole Burning in Rare-Earth Doped Crystals. *Opt. Express*
27 **2017**, *25*(13), 15539. <https://doi.org/10.1364/OE.25.015539>.
28
29 (46) Zhang, S.; Galland, N.; Lučić, N.; Le Targat, R.; Ferrier, A.; Goldner, P.; Fang, B.; Le
30 Coq, Y.; Seidelin, S. Inhomogeneous Response of an Ion Ensemble from Mechanical
31 Stress. *Phys. Rev. Res.* **2020**, *2*(1), 013306.
32 <https://doi.org/10.1103/PhysRevResearch.2.013306>.
33
34 (47) Könz, F.; Sun, Y.; Thiel, C. W.; Cone, R. L.; Equall, R. W.; Hutcheson, R. L.; Macfarlane,
35 R. M. Temperature and Concentration Dependence of Optical Dephasing, Spectral-Hole
36 Lifetime, and Anisotropic Absorption in $\text{Eu}^{3+}:\text{Y}_2\text{SiO}_5$. *Phys. Rev. B* **2003**, *68*(8),
37 085109. <https://doi.org/10.1103/PhysRevB.68.085109>.
38
39
40
41
42
43
44
45
46
47
48
49
50
51
52
53
54
55
56
57
58
59
60